行政院國家科學委員會專題研究計畫　成果報告

地震波傳遞和全球走時層析成像：香蕉－甜甜圈理論(II)

計畫類別：個別型計畫
計畫編號：NSC91-2119-M-002-027-
執行期間：91 年 08 月 01 日至 92 年 07 月 31 日
執行單位：國立臺灣大學地質科學系暨研究所

計畫主持人：洪淑蕙

計畫參與人員：喬凌雲

報告類型：精簡報告
報告附件：出席國際會議研究心得報告及發表論文
處理方式：本計畫可公開查詢

中　華　民　國 93 年 2 月 11 日

行政院國家科學委員會補助專題研究計畫成果報告

※※※※※※※※※※※※※※※※※※※※※※※※※※
※　　　　　　　　　　　　　　　　　　　　　　　　※

※地震波傳遞和全球走時層析成像：香蕉-甜甜圈理論 (II)※

※　　　　　　　　　　　　　　　　　　　　　　　　※
※※※※※※※※※※※※※※※※※※※※※※※※※※

計畫類別：∨個別型計畫　　□整合型計畫
計畫編號：NSC　91－2119－M－002－027
執行期間：　91 年 8 月 1 日至 92 年 7 月 31 日

計畫主持人：洪淑蕙
共同主持人：
計畫參與人員：喬凌雲

本成果報告包括以下應繳交之附件：
□赴國外出差或研習心得報告一份
□赴大陸地區出差或研習心得報告一份
∨出席國際學術會議心得報告及發表之論文各一份
□國際合作研究計畫國外研究報告書一份

執行單位：台灣大學地質科學系

中　華　民　國　　92 年　　10 月　　29　日

中文摘要

此研究結合長周期(25 秒爲主)的波形所測量的 S-SKS 和 ScS-S 對於標準一維地球模型 PREM 的走時差殘餘值，共同推演地涵最底部 500 公里的三維速度構造。由於地震波僅具有限頻寬，波相走時除了受構造的速度變化影響之外，還會因有限頻寬的繞射現象，造成波前後復原的現象。因此根據層析成像原理，除了以假設地震波爲無限高頻的一維線性波線理論來正演波相走時和震波速度構造的關係之外，此研究並採用近年來新發展的香蕉甜甜圈理論作爲建立反演資料核(data kernel)的依據，因該論正確地考慮走時受波前復原影響的效應，將有助於改善全球核涵邊界的解析度。同時，在模型參數化的技術上易加入多重尺度解析的觀念，由走時資料本身採樣疏密的程度，客觀評析對每一區域速度構造解析的能力。研究結果發現以有限頻寬算核所得的層析成像模型，其剪力波的側向速度異常強度要比以傳統波線理論求得的模型要大至兩倍左右。顯示過去對核涵邊界 D”層不均質的程度可能低估，連帶可能影響該層溫度、化學組成以及動力學上的解釋。D”層速度構造以 Degree 2 的變化爲主，在中太平洋和非洲底下各出現慢的速度異常，地表熱點火山活動的位置大致落於這些區域，環太平洋區域則是相對快速異常的區域，顯示和隱沒的古海洋板塊物質有關。

關鍵詞：有限頻寬走時層析成像、剪力波異常、核涵邊界、D”層、多重尺度模型參數化。

Abstract. We present the global distribution of shear velocity heterogeneity in the lowermost 500 km of the mantle derived from a joint inversion of differential S (or diffracted S)-SKS and ScS-S travel-time residuals measured by long-period waveforms dominant at 25 s. Fréchet or banana-doughnut kernel theory is utilized to forward modeling of finite-frequency travel-time measurements. A model parameterization based on a multiresolution wavelet representation is implemented to inversely solve for spatial variations in mantle shear wavespeed perturbations. The resolved velocity heterogeneity strength is about twice as much as that in the previous model

constrained by similar dataset but ray-obtained tomography. Surface hotspots in the Central Pacific and the Indian-Africa are correlated with deep-rooted mantle plumes located within or on the edge of broad, low-velocity D" regions. Relatively fast velocity structures that underlie beneath the Circum-Pacific Rim are associated with ancient cold subducted materials.

Key words: finite-frequency traveltime tomography, shear velocity heterogeneity, core-mantle boundary, D" layer, multiscale model parameterization

1. Introduction

Lateral variation in shear velocity perturbations near the core-mantle boundary (CMB) or in D" zone has been unraveled exclusively by the traveltimes of diffracted S waves. From an infinite-frequency ray-theoretical point of view, the Sd wave emerging in the core shadow uniquely samples the grazing ray segment along the CMB. Synthetic experiment suggests that the traveltime shift measured by an actual finite-frequency wave can differ substantially from the prediction of ray theory because of intrinsic wavefront healing effects (*Hung et al*., 2001; *Baig et al*., 2001). Lately Fréechet kernel theory based on Born single scattering approximation has been developed to correct such deficiency (*Dahlen et al*., 2000; *Zhao et al*., 2000). A S traveltime residual yields unexpectedly zero sensitivity right on the geometrical raypath; rather, it is most sensitive to the surrounding off-path heterogeneity. The SHd traveltime kernel exhibits even paradoxical features on the CMB where the Sd ray glides; it has the opposite (or positive) sign suggesting that a Sd arrival could speed up by a slow anomaly at the CMB.

Constrained mostly by compelling seismic evidence, the remote D" zone is thought to be one of the most heterogeneous and dynamic region in the earth's interior. Recent ray-based tomographic inversion of long-period differential S(or Sd)-SKS traveltimes revealed a global distribution of anomalous D" shear velocity on the scale length > ~1000 km (*Kuo et al*., 2000). To assess the potential bias of the resolved D" structure due to inadequate interpretation of finite-frequency arrivals, we conduct a tomographic study of global mantle shear velocity heterogeneity using both 1-D ray theory and 3-D banana-doughnut kernels. A

computationally-efficient paraxial formulation based upon body-wave propagation together with full wave theory is implemented to construct the kernels for finite-frequency differential traveltime measurements. We discuss the difference among the resulting models as a result of wave diffraction and model parameterization.

2. Data and Method

Prior to differential traveltime measurements, all the teleseismic broadband waveforms are filtered to the LP response of the GDSN (Global Digital Seismic Network) data. Differential S (or Sd)-SKS and ScS-S traveltimes relative to the arrivals predicted by 1-D reference PREM model are determined by shifted time lags required to match the initial swing of the waveforms in a pair of phase arrivals. For a given differential traveltime residual δt that relates to shear velocity perturbation in the mantle, the conventional ray-theoretical formulation is simply

$$\delta t = \int_{ray} \left(\frac{-1}{\beta} \right) \left(\frac{\delta \beta}{\beta} \right) dl \,, \qquad (1)$$

that is, integral of the slowness (or the reciprocal of velocity) perturbation, $\delta\beta/\beta$, along the geometrical ray path in the radially-symmetric PREM model. On the other hand, finite-frequency kernel theory expresses the relation between δt and $\delta\beta/\beta$ in a 3-D volumetric integral within the Earth's mantle, Ω (e.g., *Dahlen et al*., 2000),

$$\delta t = \int_{\Omega} K(r,\theta,\phi) \frac{\delta \beta}{\beta} dV \qquad (2)$$

With (r,θ,ϕ) denoting the 3-D spherical coordinates, *K* represents the kernel function and $\delta\beta/\beta$ is the shear velocity perturbation at (r,θ,ϕ) within an infinitesimal volume, *dV*. In practice, numerical integration of eq (2) within a single voxel is achieved by the weighted sum of limited sampling points according to the Gaussian quadrature formulation (e.g., *Zienkiewicz and Taylor*, 1989). Contribution from all voxels are then summed up to form the data equation of the form,

$$\delta t_i = d_i = G_{ij} m_j . \qquad (3)$$

Our data used for multiscale finite-frequency tomography consists of 1568 S-SKS residuals compiled by *Kuo et al*. (2000) who grouped the residuals from redundantly sampled regions to minimize uneven path coverage (Figure 1a). Additional 8256 ScS-S residuals from *Masters et al*. (2000) are also included in the traveltime inversion (Figure 1b).

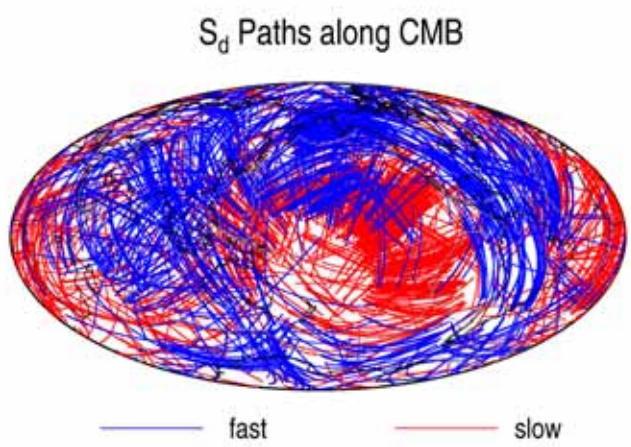

Figure 1. (a) Segments of Sd ray paths within a 250-km-thick D" layer. Red colors represent positive Sd-SKS residuals or slower differential arrivals relative to those in the PREM model, while blue colors are negative residuals or relatively faster arrivals.

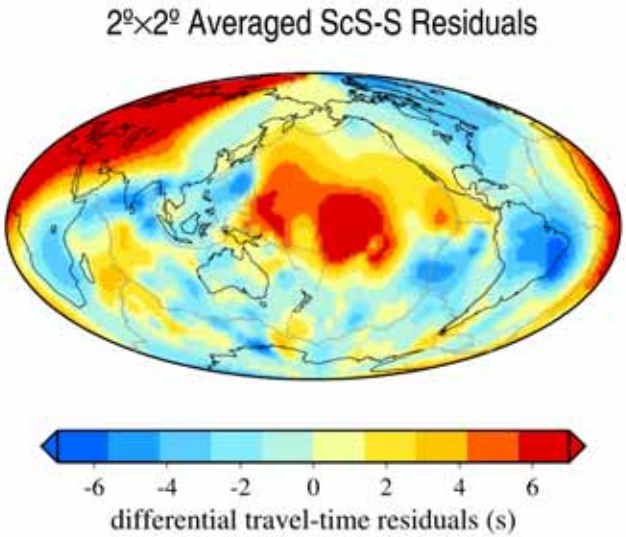

Figure 1(b). The 2o cap-averaged ScS-S residuals showing long-wavelength velocity variations in the reflection points.

Figure 2 shows cross-sectional views of the 3-D sensitivity kernels for an example Sd-SKS and ScS-S residual measurement. The whole mantle is divided into 32 equally-spacing layers in radial direction and 5120 almost equal-area spherical triangles in lateral dimensions. Shear velocity perturbations are parameterized in terms of spherical blocks and multiscale representation that invokes the biorthogonal generalized Harr wavelets on a sphere (*Chiao and Kuo*, 2001; *Chiao and Liang*, 2002) (Figure 1c).

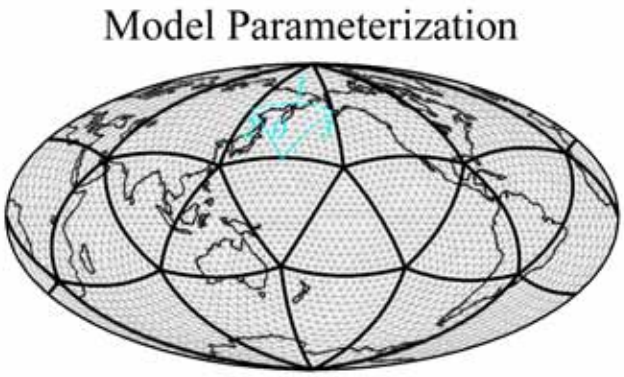

Figure 1(c). Model parameterization used in the traveltime tomography. Construction of spherical wavelets starts with a regular geodesic polyhedron (e.g., icosahedron) and successive refinement by subdividing each spherical triangle into four children up to the refinement level 5. It leads to totally 5120 spherical triangles.

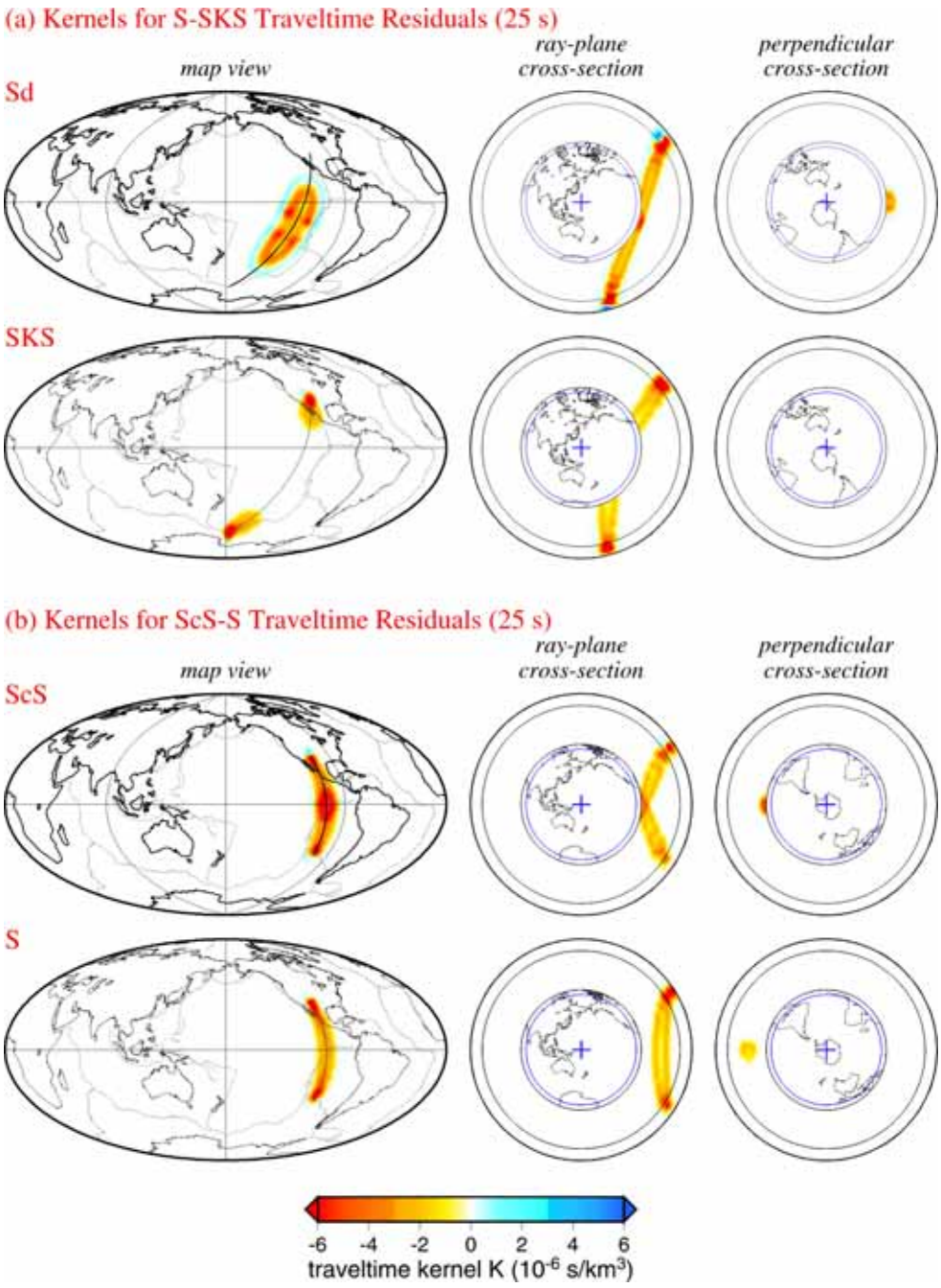

Figure 2. (a) Finite-frequency traveltime kernels for Sd and SKS waves with a dominant period of 25 s at an epicentral distance $\Delta = 114^{o}$. The kernel for a differential Sd-SKS traveltime residual is the difference of the individual Sd and SKS kernels. On map view shows the Sd kernel near CMB. (b) Finite-frequency traveltime kernels for ScS and S waves with a dominant period of 25 s at an epicentral distance $\Delta = 71^{o}$. The kernel for a ScS-S residual is the difference of the individual ScS and S kernels. The maximum amplitude of the kernel is projected on map view.

3. Result

Because the sensitivity kernel K in eq~(2) is founded on the assumption that a differential traveltime residual is measured by cross-correlation of two observed waveform pulses, slightly different from the initial-swing time-shift measurements used for the S-SKS and ScS-S data. The latter approach is introduced by *Masters et al*., (1996) to improve the effective spatial resolution their traveltime measurements, by emphasizing the high-frequency components of an observed pulse. *Hung et al*., (2001) conducted a synthetic test of the traveltime shifts induced by a single spherical velocity anomaly and made comparison of the measurements obtained from these two methods. They found that the first-swing measurements did reduce the effects of wavefront healing; thereby reducing ~60% in the effective period, from 25 s to 15 s. Therefore, we present the finite-frequency tomographic models obtained with the traveltime sensitivity derived from the 25-s and 15-s kernels. Figure 3 compares relative sampling density among these three data kernels, that is, linearized ray, 25-s kernel and 15-s kernel.

Figure 4 compares shear velocity perturbations in the lowermost mantle obtained with infinite-frequency ray and 25-s and 15-s finite-frequency tomography. All the three models are parameterized by spherical triangular blocks. Obviously, the velocity variation in the ray-based model tends to be restrained on the unevenly-sampling raypaths and yields many short-wavelength, rough features superimposed on a dominant degree 2 pattern. The power spectrum is substantially lost in the damped least-squares solution to maintain the spatial resolution. Because of the natural widespread off-path sensitivity for finite-frequency traveltimes, the kernel-derived model is comparatively smoother. Moreover, the 3-D kernels account for wavefront healing and other finite-frequency diffractive effects; thus the magnitude of resolved velocity perturbations increases by a factor of 2.

Figure 5 uses the same data kernels as those in Figure 4, while the model is alternatively parameterized in terms of multiresolution representation using spherical Harr wavelets. The wavelet-based multiscale parameterization builds a natural regularization scheme based on actual

raypath sampling to extract well-constrained structures without sacrificing the spectral resolution. Therefore, S-wave velocity structure near the CMB is dominated by lateral variations in degree 2 with the relatively slow anomaly beneath the Central Pacific and Africa surrounded by the fast anomaly.

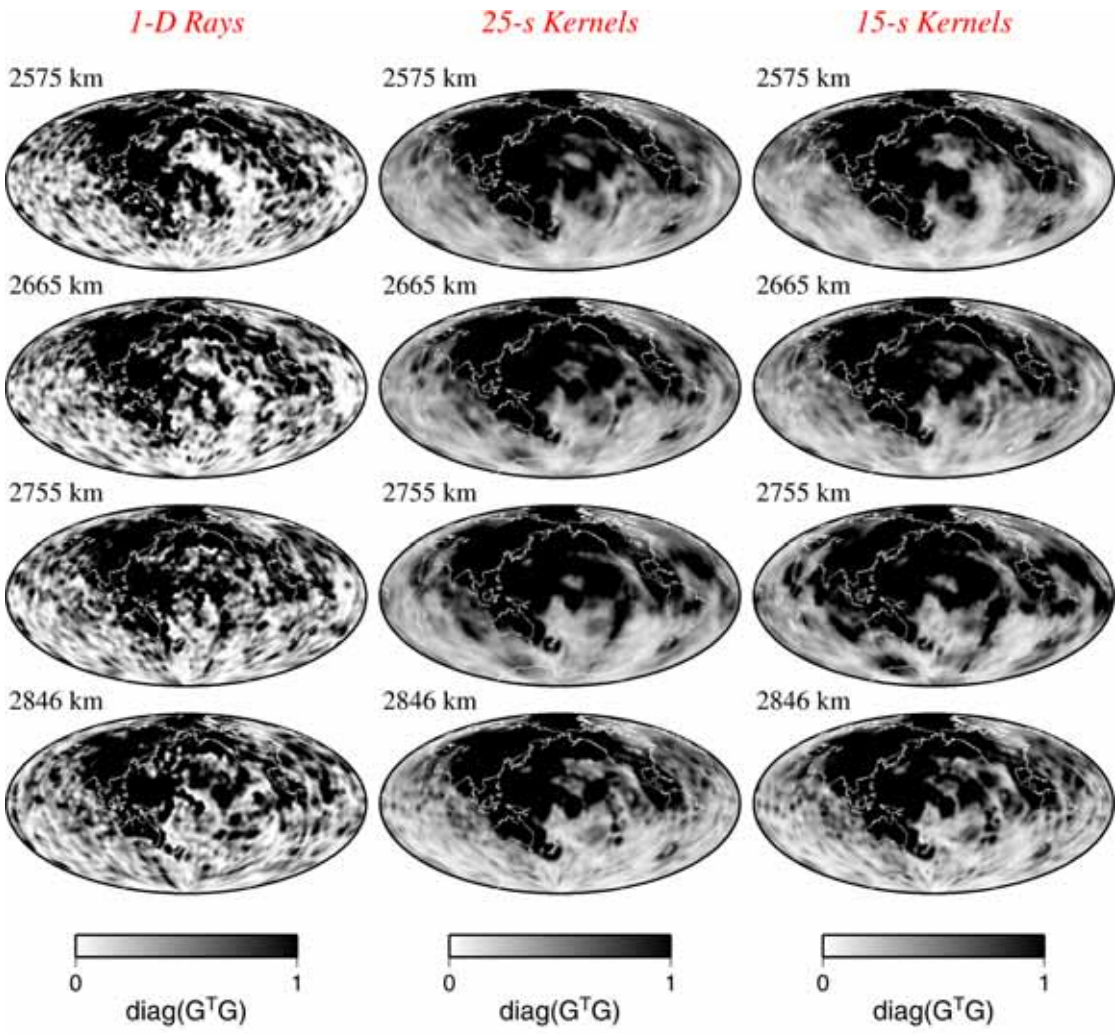

Figure 3. Comparison of samping density of 1-D ray and volumetric kernels.

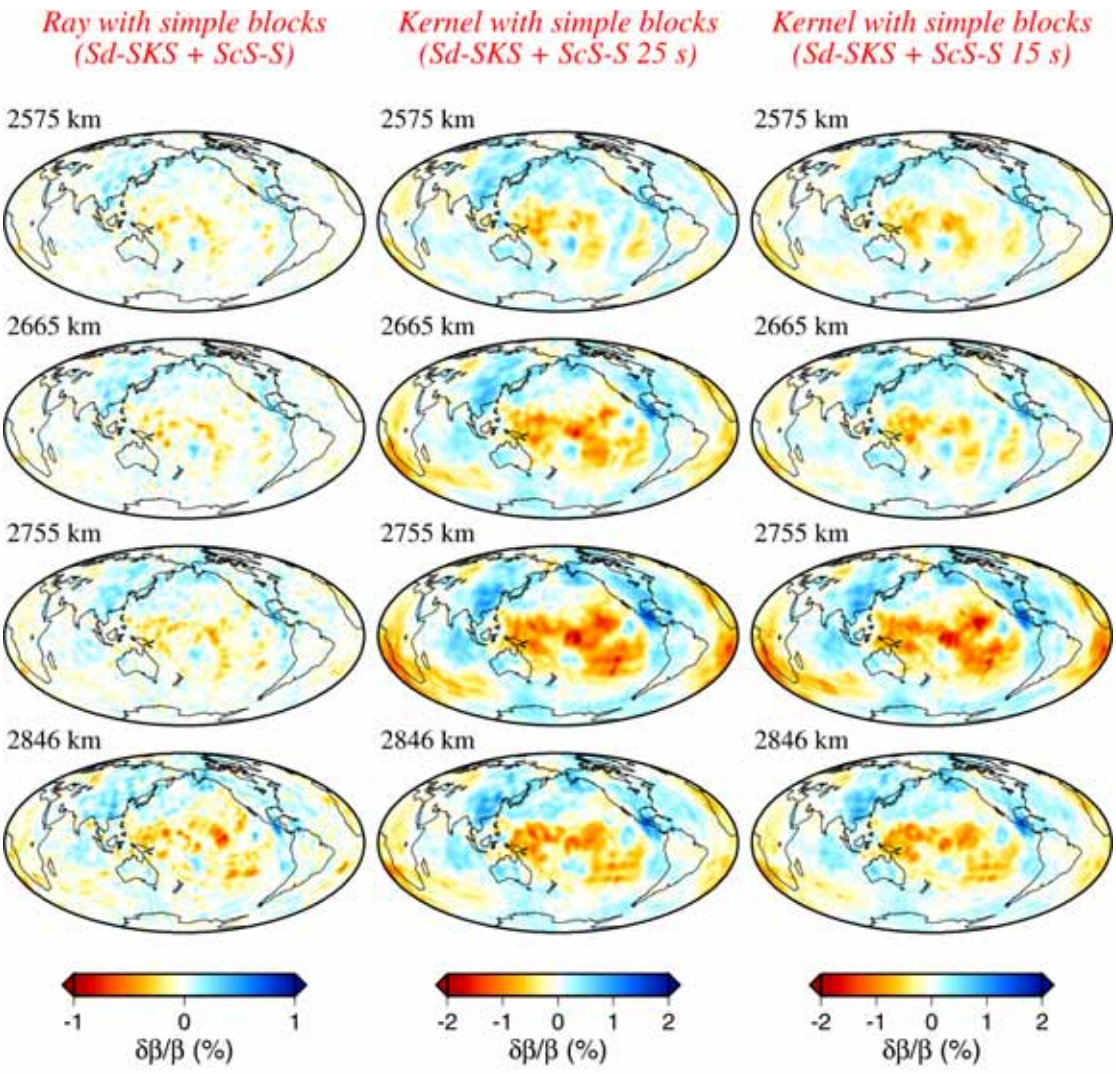

Figure 4. Comparison of shear velocity perturbations near CMB resolved from traveltime tomography. The data kernel that governs the relation between model (velocity or slowness perturbation) and data (residuals) is built based upon ray theory and 3-D kernels of a finite-frequency wave with a dominant period of 25 and 15 s. All the three models are parameterized by spherical blocks or pixels.}

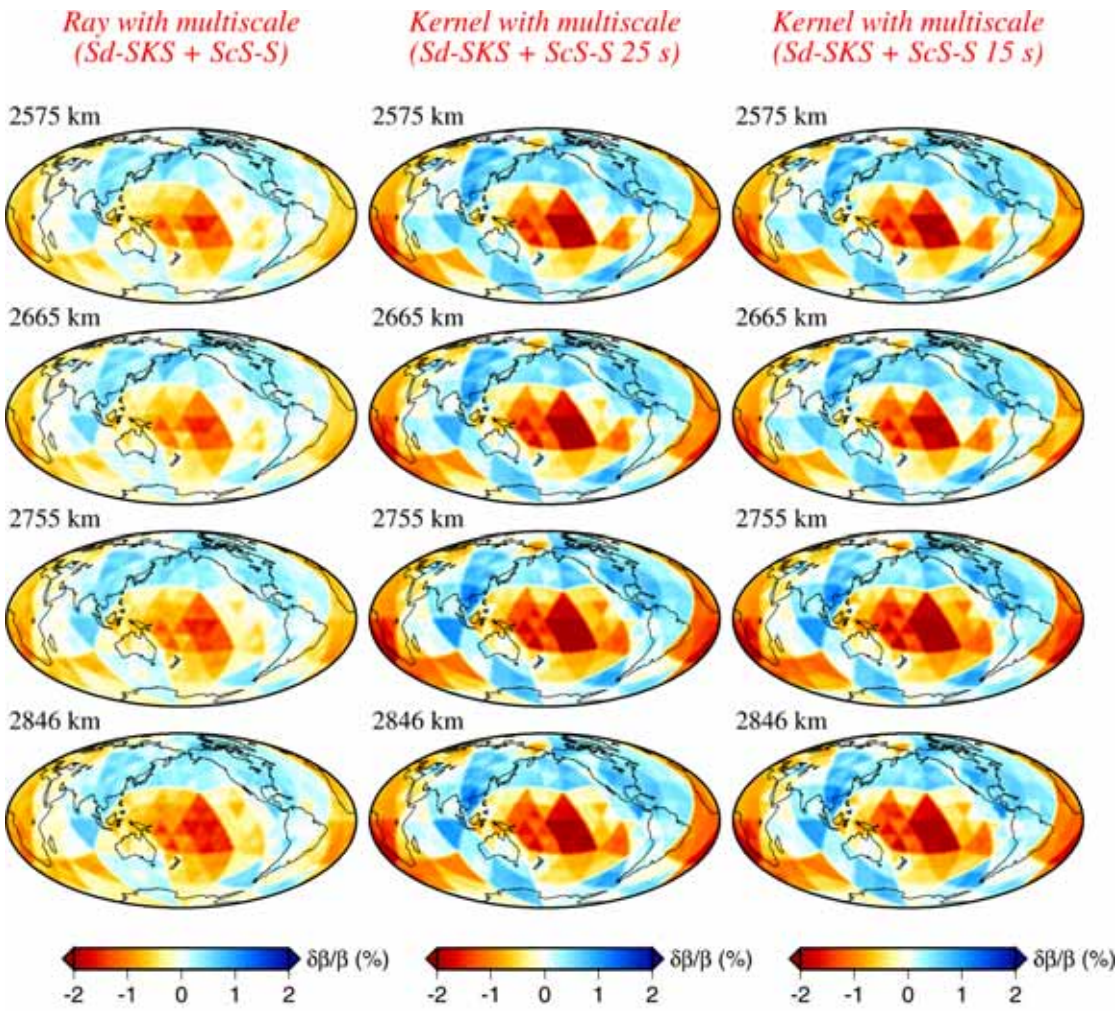

Figure 5. Comparison of shear velocity perturbations near CMB resolved from ScS-S and S-SKS traveltime tomography. The data kernel is constructed in the same way as that done in block-based inversion, while the model is alternatively parameterized in terms of multiresolution representation using spherical Harr wavelets.

4. Conclusion

Several conclusions can be drawn in this study:

1. Given similar variance reductions, the 3-D kernel inversion yields smoother models with much larger velocity perturbations. than those ray-based models.

2. The smoothing may arise from the off-path sensitivity of actual finite-frequency traveltimes as revealed from the 3-D kernel. The whole mantle heterogeneity inferred from all the contemporary 3D earth models is probably underestimated because wavefront healing is completely neglected in

the ray approach.

3. Multiscale inversions suggest that the current S (or Sd)-SKS and ScS-S residuals only resolve the robust features in long-wavelength, degree 2 variations.

References

Baig, A.M., F.A. Dahlen, and S.-H. Hung, Traveltimes of waves in three-dimensional random media, *Geophys. J. Int*., 153, 467--482, 2003.

Chiao, L.-Y., and B.-Y. Kuo, Multiscale seismic tomography, *Geophys. J. Int*., 145, 517--527, 2001.

Chiao, L.-Y., and W.-C. Liang, Multiresolution parameterization for geophysical inverse problems, *Geophysics*, 145, 517--527, 2003.

Cohen A., I. Daubechies, and J.-C. Feauveau, Biorthogonal bases of compactly supported wavelets, *Comm. Pure Appl. Math.*, 45, 485--560, 1992.

Dahlen, F.A., S.-H. Hung, and G. Nolet, Fr\'{e}chet kernels for finite-frequency traveltimes -- I. Theory, *Geophys. J. Int*., 141, 157--174, 2000.

Hung, S.-H., and D.W. Forsyth, Modeling anisotropic wave propagation in oceanic inhomogeneous structures using the parallel multi-domain pseudospectral method, *Geophys. J. Int*., 133, 726--740, 1998.

Hung, S.-H., F.A. Dahlen, and G. Nolet, Fréchet kernels for finite-frequency traveltimes -- II. Examples, *Geophys. J. Int*., 141, 175--203, 2000.

Hung, S.-H., F.A. Dahlen, and G. Nolet, Wavefront healing: a banana-doughnut perspective,*Geophys. J. Int*., 146, 289--312, 2001.

Kuo, B.-Y., and K.-Y., Wu, Global shear velocity heterogeneities in the D" layer: Inversion from Sd-SKS differential travel times, *J. Geophys. Res.*, 102, 11,775--11,788, 1997.

Kuo B.-Y., E.J. Garnero, and T. Lay, Tomographic inversion of S-SKS times for shear velocity heterogeneity in D": Degree 12 and hybrid models, *J. Geophys. Res.*, 105, 28,139--28,158, 2000.

Mallat, S., Multiresolution approximations and wavelet orthonormal bases of L2(R), *Trans. Am. Math. Soc.*, 315, 69--88, 1989a.

Mallat, S., A theory of multiresoultion signal decomposition: the wavelet representation, *IEEE Transactions on Pattern Analysis and Machine Intelligence,* 11, 674--693, 1989b.

Masters, G., S. Johnson, G. Laske, and H. Bolton, A shear-velocity model of the mantle, *Phil. Trans. R. Soc. Lond.*, 354, 1385--1411, 1996.

Schroder, P., and W. Sweldens, Spherical wavelets: Efficiently representing functions on the sphere, *SIGGRAPH: Computer Graphics Proceedings, Annual Conference Series,* 161--172, 1995.

Sweldens, W., The lifting scheme: Accustom-design construction of biorthogonal wavelets, *Appl. Comput. Harmon. Anal.*, 3, 186--200, 1996.

Zhao, L., T.H. Jordan, and C.H. Chapman, Three-dimensional Fr\'{e}chet differential kernels for seismic delay times, *Geophys. J. Int*., 141, 558--576, 2000.

Zienkiewicz, O.C., and R.L. Taylor, *The Finite Element Method: Vol I, Basic formulation and Linear Problems*, 4th ed., pp. 648, McGraw-Hill, Singapore, 1989.

Supplement Materials

1. Published paper related to this project
   Montelli, R., G. Guust, F.A. Dahlen, G. Masters, E.R. Engdahl, and S.-H. Hung, Finite-frequency tomography reveals a variety of plumes in the mantle, *Science*, 303, 338-343, 2004.
2. The results presented in the report was presented in 2001 Fall AGU meeting held in San Francisco, USA.
   Hung, S.-H., L.-Y. Chiao, B.-Y. Kuo, and F.A. Dahlen, Diffraction tomography of shear velocity heterogeneity in the lowermost mantle, *AGU Fall Meeting Suppl.*, 82, F1129, 2001.

T21A-0843 0830h POSTER

Diffraction Tomography of Shear Velocity Heterogeneity in the Lowermost Mantle

S.-H. Hung[1] (886-2-23630231: shung@ccms.ntu.edu.tw)
L.-Y. Chiao[2]
B.-Y. Kuo[3]
F.A. Dahlen[4]
[1]National Taiwan University, Department of Geosciences, Taipei 106, Taiwan
[2]Nation Taiwan University, Institute of Oceanography, Taipei 106, Taiwan
[3]Academia Sinica, Institute of Earth Sciences, Taipei 115, Taiwan
[4]Princeton University, Deperatment of Geosciences, Princeton, NJ 08544, United States

Lateral variation in shear velocity perturbations near the core-mantle boundary (CMB) has been unraveled exclusively by traveltimes of diffracted S waves. From an infinite-frequency ray-theoretical point of view, the S_d wave emerging in the core shadow uniquely samples the grazing ray segment along the time shift measured by an actual finite-frequency wave can differ substantially from the prediction of ray theory because of intrinsic wavefront healing effects. The Fréchet kernel theory based on the Born single scattering approximation is developed lately to correct such deficiency. A S traveltime residual yields unexpectedly zero sensitivity right at the geometrical ray; rather, it is most sensitive to the surrounding off-path heterogeneity. The SH_d traveltime kernel exhibits even paradoxical features on the CMB where the S_d ray glides; it has the opposite (or positive) sign suggesting that a S_d arrival could speed up by a slow anomaly at the CMB.

Constrained mostly by compelling seismic evidence, the remote D" zone is thought to be one of the most heterogeneous and dynamic region in the earth's interior. Recent ray-based tomographic inversion of long period differential S (or Sd)-SKS traveltimes revealed a global distribution of anomalous D" shear velocity on the scale length >~1000Km. To access the potential bias of the resolved D" structure due to inadequate interpretation of finite-frequency arrivals, we will insert the S-SKS dataset using the 3D kernels. The model is parameterized by both the common block and multiscale scheme that invokes spherical wavelets. A computationally-efficient paraxial formulation based upon body-wave propagation together with full wave theory is implemented to construct the S_d and SKS kernels. This study will discuss the plausible difference between the kernel and ray based results. In consistency among the models arising from imperfect parameterization for nonuniform data coverage will be also addressed.

S32B-0636 1330h POSTER

Global Time Tomography of Finite Frequency Waves with Optimized Tetrahedral Grids.

Raffaella Montelli[1,2] (609-258-1505; montelli@princeton.edu)
Guust Nolet[1] (nolet@princeton.edu)
Francis Anthony Dahlen[1] (fad@princeton.edu)
Guy Masters[3] (guy@mahi.ucsd.edu)
Shu-Huei Hung[4] (shung@ccms.ntu.edu.tw)
[1] Department of Geosciences, Guyot Hall Princeton University, Princeton, NJ 08540, United States.
[2] CNRS-UNSA Géosciences Azur, 215 rue A. Einstein Sophia Antipolis, Valbonne 06560, France
[3] IGPP, U.C. San Diego, La Jolla, CA 92093, United states
4 Department of Geosciences, National Taiwan University, Taipei, Taiwan

Besides true velocity heterogeneities, tomographic images reflect the effect of data errors, model parameterization, linearization, uncertainties involved with the solution of the forward problem and the greatly inadequate sampling of the earth by seismic rays. These influences cannot be easily separated and often produces artefacts in the final image with amplitudes comparable to those of the velocity heterogeneities. In practices, the tomographer uses some form of damping of the ill-resolved aspects of the model to get a unique solution and reduce the influence of the errors. However damping is not fully adequate, and may reveal a strong influence of the ray path coverage in tomographic images. If some cells are ill determined regularization techniques may lead to heterogeneity because these cells are damped towards zero. Thus we want a uniform resolution of the parameters in our model. This can be obtained by using an irregular grid with variable length scales.

We have introduced an irregular parameterization of the velocity structure by using as delaunay triangulation. Extensively work on error analysis of tomographic images together with mesh optimization has shown that both resolution and ray density can provide the critical information needed to re-design grids. However, criteria based on resolution are preferred in the presence of narrow ray beams coming from the same direction. This can be understood if we realize that resolution is not only determined by the number of rays crossing a region, but also by their azimutal coverage. We shall discuss various strategies for grid optimization.

In general the computation of the travel times is restricted to ray theory, the infinite frequency approximation of the elastodynamic equation of motion. This simplifies the mathematic and is therefore widely applied in seismic tomography. But ray theory does not account for scattering, wavefront healing and other diffraction effects that render the travel time of a finite frequency

seismic waves sensitive to three-dimensional-structure off ray.

Dahlen et al (2000) used the Born approximation to find a double-ray sum representation of the 3D Fréchet kernel. Destructive interference among adjacent frequencies in the board-band pulse render a cross-correlation traveltime measurement sensitive only to the wave speed in an hallow banana-shaped region combined the banana-doughnut kernel with the formalism for the adaptive parameterization based on resolution criterion for a long-period body wave data set.

Both absolute and differential times are computed using cross0correlation of each observed arrival with a synthetic pulse constructed by convolving the impulse and an attenuation operator for the preliminary reference earth model (PREM).

We shall present some first results illustrating the effects of using banana-doughnut Fréchet kernels instead of ray theory on the construction of optimized Delaunay meshs.

S32c-0640 1330h POSTER

Validation of Born Traveltime Kernels

Adam M Baig[1] (609-258-1504; abaig@princeton.edu)
F. A. Dahlen[1] (609-258-4130; fad@princeton.edu)
Shu-Heui Hung[1] (Shung@ccms.ntu.edu.tw)
[1]Department of Geosciences, Princeton University, Princeton, NJ 08554, United States

Most inversions for Earth structure using seismic traveltimes rely on linear ray theory to translate observed traveltime anomalies into seismic velocity anomalies distributed throughout the mantle. However, ray theory is not an appropriate tool to use when velocity anomalies have scale lengths less than the width of the Fresnel zone. In the presence of these structures, we need to turn to a scattering theory in order to adequately describe all of the features observed in the waveform. By coupling the Born approximation to ray theory, the first order dependence of heterogeneity on the cross-correlated traveltimes (described by the Fréchet derivative or, more colorfully, the banana doughnut kernel) may be determined.

To determine for what range of parameters these banana-doughnut kernels outperform linear ray theory, we generate several random media specified by their statistical properties, namely the RMS showness perturbation and the scale length of the heterogeneity. Acoustic waves are numerically generated from a point source using a 3-D pseudo-spectral wave propagation code. These waves are then recorded at a variety of propagation distances from the source introducing a third parameter to the problem: the number of wave lengths traversed by the wave. When all of the heterogeneity has scale lengths larger than the width of the Fresnel zone, ray theory does as good as the banana-doughnut kernels do. Below this limit, Waveform healing becomes a significant effect and ray theory ceases to be effective even though the kernels remain relatively accurate a given regime.

The study of wave propagation in random media is of a more general interest and we will also show our measurements of the velocity shift and the variance of teaveltime compare to various theoretical predictions in a given regimes.

rejection of many sources of noise and error, should hold promise for ultimately accomplishing mass comparisons at 1×10^{-12} or 2×10^{-12}. For a molecule with mass 30 u, such precision would provide an energy resolution of 0.03 eV, allowing direct weighing of chemical binding energies to a few percent. This would be a new tool to investigate simple ionic species not amenable to conventional spectroscopic and thermochemical techniques.

References and Notes

1. M. P. Bradley, J. V. Porto, S. Rainville, J. K. Thompson, D. E. Pritchard, *Phys. Rev. Lett.* **83**, 4510 (1999).
2. A. Wicht, J. M. Hensley, E. Sarajlic, S. Chu, *Phys. Scr.* **T102**, 82 (2002).
3. E. Kruger, W. Nistler, W. Weirauch, *Metrologia* **35**, 203 (1998).
4. G. Gabrielse *et al.*, *Phys. Rev. Lett.* **82**, 3198 (1999).
5. B. Fogelberg, K. A. Mezilev, H. Mach, V. I. Isakov, J. Slivova, *Phys. Rev. Lett.* **82**, 1823 (1999).
6. F. DiFilippo, V. Natarajan, K. R. Boyce, D. E. Pritchard, *Phys. Rev. Lett.* **73**, 1481 (1994).
7. A. Marshall, C. L. Hendrickson, G. S. Jackson, *Mass Spectrom. Rev.* **17**, 1 (1998).
8. G. Siuzdak, *The Expanding Role of Mass Spectrometry in Biotechnology* (MCC Press, San Diego, CA, 2003).
9. G. L. Greene, M. S. Dewey, E. G. Kessler, E. Fischbach, *Phys. Rev. D* **44**, R2216 (1991).
10. V. M. Lobashev, *Nucl. Phys. A* **A719**, 153c (2003).
11. J. K. Thompson, S. Rainville, D. E. Pritchard, in preparation.
12. R. S. Van Dyck, D. L. Farnham, S. L. Zafonte, P. B. Schwinberg, *Rev. Sci. Instrum.* **70**, 1665 (1999).
13. I. Bergstrom *et al.*, *Nucl. Instrum. Methods A* **487**, 618 (2002).
14. T. Beier *et al.*, *Phys. Rev. Lett.* **88**, 011603 (2002).
15. E. A. Cornell, K. R. Boyce, D. L. K. Fygenson, D. E. Pritchard, *Phys. Rev. A* **45**, 3049 (1992).
16. S. Rainville, thesis, Massachusetts Institute of Technology, Cambridge, MA (2003).
17. Measured molecular binding energies are used to determine the atomic mass of neutral atoms from our measured molecular mass ratios. The uncertainty on the molecular binding energies only limits the accuracy of the neutral atomic mass to a few parts in 10^{12}, because for most molecules, the binding energies typically represent a correction of a few parts in 10^{10}, and they are known to better than a few percent. For molecules with poorly measured binding energies, mass comparisons can be used to directly weigh the chemical binding energy, as discussed in the text.
18. L. S. Brown, G. Gabrielse, *Rev. Mod. Phys.* **58**, 233 (1986).
19. The measured magnetic field inhomogeneities after shimming are $B_2 = 6.1(6) \times 10^{-9} B_0/\mathrm{mm}^2$ and $B_4 = 1.2(5) \times 10^{-9} B_0/\mathrm{mm}^4$, where $B_0 = 8.53$ T. The measured electrostatic anharmonicity is $C_6 = 0.0011(1)$. The value of C_4 is varied using the guard ring electrodes located between the endcap and the ring electrodes. The C_4 was purposely set to values of $|C_4| \leq 1.5 \times 10^{-4}$ for reasons described in the text, but could be zeroed to $\pm 4 \times 10^{-6}$ if desired.
20. For phase-sensitive detection of the axial mode, the image currents that each ion's axial motion induces across the trap electrodes are coupled to a dc superconducting quantum interference device via a superconducting self-resonant transformer (with a quality factor of about 47,000).
21. J. K. Thompson, thesis, Massachusetts Institute of Technology, Cambridge, MA (2003).
22. The canonical angular momentum can also be transferred from the separation mode to the common mode by placing the fixed axial drive above the axial resonance, thereby changing the phase of the magnetron frequency modulation by π and making ρ_s decrease while ρ_{com} increases.
23. Even if the common mode amplitude is not precisely zeroed, the beating of the two collective modes will lead to time averaging of the radially dependent magnetic field inhomogeneities on a time scale much shorter than the one needed for a typical cyclotron frequency comparison.
24. E. A. Cornell, R. M. Weisskoff, K. R. Boyce, D. E. Pritchard, *Phys. Rev. A* **41**, 312 (1990).
25. Only at the smallest ion-ion separations of $\rho_s \leq 500$ μm is the perturbation of the measured axial frequency significant enough to affect the measured cyclotron frequency ratio at 10^{-11}.
26. The sign of the originally predicted shift [eq. 4-14 in (*15*)] was found to be incorrect.
27. The measured ratio has not shown any systematic variation with ρ_s either in three preliminary data sets using different molecules.
28. There is no polarization shift of the cyclotron frequency of $^{13}C_2H_2^+$ at the current level of precision, because the ion has zero effective dipole moment in its linear electronic ground state (*11*, *34*).
29. M. W. Chase, *J. Phys. Chem. Ref. Data* **9**, 1 (1998).
30. P. Linstrom, W. Mallard, Eds., NIST Chemistry WebBook, NIST Standard Reference Database Number 69, March 2003 Release (National Institute of Standards and Technology, Gaithersburg, MD, 20899) (http://webbook.nist.gov).
31. R. S. VanDyck, S. L. Zafonte, P. B. Schwinberg, *Hyperfine Interact.* **132**, 163 (2001).
32. V. Natarajan, F. DiFilippo, D. E. Pritchard, *Phys. Rev. Lett.* **74**, 2855 (1995).
33. S. Rainville, M. P. Bradley, J. V. Porto, J. K. Thompson, D. E. Pritchard, *Hyperfine Interact.* **132**, 177 (2001).
34. M. F. Jagod *et al.*, *J. Chem. Phys.* **97**, 7111 (1992).

35. We acknowledge with gratitude that the experimental and measurement technologies that have made these experiments possible are the result of about 20 years of effort by previous group members, especially the detector technology developed by M. P. Bradley and J. V. Porto. We thank E. G. Myers for many helpful comments on the manuscript. This work was supported by NSF and was formerly supported by the National Institute of Science and Technology and the Joint Services Electronics Program. S.R. acknowledges the support of the Fonds pour la Formation de Chercheur et l'Aide à la Recherche.

7 October 2003; accepted 18 November 2003
Published online 11 December 2003;
10.1126/science.1092320
Include this information when citing this paper.

Finite-Frequency Tomography Reveals a Variety of Plumes in the Mantle

Raffaella Montelli,[1]* Guust Nolet,[1] F. A. Dahlen,[1] Guy Masters,[2] E. Robert Engdahl,[3] Shu-Huei Hung[4]

We present tomographic evidence for the existence of deep-mantle thermal convection plumes. *P*-wave velocity images show at least six well-resolved plumes that extend into the lowermost mantle: Ascension, Azores, Canary, Easter, Samoa, and Tahiti. Other less well-resolved plumes, including Hawaii, may also reach the lowermost mantle. We also see several plumes that are mostly confined to the upper mantle, suggesting that convection may be partially separated into two depth regimes. All of the observed plumes have diameters of several hundred kilometers, indicating that plumes convey a substantial fraction of the internal heat escaping from Earth.

Hotspots are characterized by higher temperature, topographic swells, and recent volcanism with isotopic signatures distinct from those that characterize mid-ocean ridge or andesitic basalts (*1*–*3*). The best known example is the Hawaii-Emperor volcanic chain, which may have formed as the Pacific plate moved over a deep magmatic source (*3*–*10*). Narrow thermal upwellings in the form of plumes are commonly observed in laboratory experiments (*11*, *12*) and numerical simulations (*13*–*15*), and deep-mantle plumes have been invoked to explain flood basalts, the isotopic signature of ocean island basalts, and the topography of the swells and plateaus that often accompany volcanic hotspots. Although this has led to a coherent (albeit incomplete) theory of much of the geology that characterizes hotspots, undisputed evidence for the existence of lower-mantle plumes in tomographic images of the mantle is lacking. High temperatures reduce the velocity of seismic waves, so that plumes should be evinced as columnar low-velocity anomalies. In the absence of convincing tomographic evidence, it has recently been argued that hotspots could instead be the manifestation of shallow, plate-related stresses that would fracture the lithosphere, causing volcanism to occur along these cracks (*16*–*18*).

The inversion. A unique feature of our tomographic inversion is the use of finite-frequency sensitivity kernels (*19*, *20*) to account for effects of wavefront healing on the travel times of low-frequency *P* waves; this enables us to combine long- and short-period data sets. We use a remeasured, expanded set of long-period data and very carefully selected short-period delay times, and we adapt the model parameterization to the lower resolution at depth. Global

[1]Department of Geosciences, Princeton University, Princeton, NJ 08544, USA. [2]Institute of Geophysics and Planetary Physics, University of California at San Diego, La Jolla, CA 92093, USA. [3]Department of Physics, University of Colorado, Boulder, CO 80309, USA. [4]Department of Geosciences, National Taiwan University, Taipei, Taiwan.

*To whom correspondence should be addressed. E-mail: montelli@princeton.edu

tomographic models of seismic *P*-wave velocity have so far relied almost exclusively on classical ray theory. In this infinite-frequency approximation, the travel time of a *P* wave is only influenced by seismic velocity along an infinitesimally narrow path—the seismic ray. This simplifies the mathematics, but it ignores sensitivity of the travel time to velocity structure off of the ray, within a volume known as the Fresnel zone (*21*). The cross-ray diameter of the Fresnel zone is on the order of $(\lambda L)^{1/2}$ for a wave of wavelength λ and ray length L, and can be in excess of 1000 km at the long periods we consider. As a result of diffractive wavefront healing, objects much smaller than the width of the Fresnel zone will not appreciably influence the travel time of the wave (*22*, *23*). For heterogeneities comparable in size to the Fresnel zone, one may account for these wavefront healing effects with the use of a new method of interpretation (*19*, *20*), which we refer to as finite-frequency tomography. A preliminary analysis of low-frequency *P*-wave arrival times shows that the amplitudes of deep, small-scale velocity heterogeneities are underestimated by 30 to 60% when interpreted by classical ray theory (*24*).

Mantle plumes are probably narrow, and their images are potentially degraded if we ignore the effects of wavefront healing (*25*). We present the result of a finite-frequency tomographic inversion based on the travel times of 66,210 *P*-waves and the differential travel times of 20,147 *PP*-*P* and 2382 *pP*-*P* waves, with a dominant period of 20 s, combined with 1,427,114 short-period *P* and 68,911 short-period *pP* travel times extracted from bulletins (*26*). The travel times of the long-period phases were measured by cross-correlation with a synthetic pulse (*27*) and were inverted using three-dimensional finite-frequency sensitivity kernels (*19*); the short-period travel times were inverted using ray theory. Although part of the long-period data set also served to construct model P16B30 (*28*), the original seismograms were reanalyzed, and previously undetected clock errors have been corrected (*29*). The standard deviations of the long-period times were assigned to three accuracy classes and range from 0.5 to 1.15 s (*24*). The short-period travel times were picked onset times reported to the International Seismological Centre (ISC) and later reinterpreted with smaller uncertainties (*30*). Of a total of 9.2 million *P* measurements, we selected only the ~16% listed with two-decimal precision. The standard deviations of the short-period times are 0.9 s for *P* and 1.1 s for *pP* (*31*); about 45,000 outliers with deviations larger than 3σ were rejected after a first iteration.

We simultaneously inverted for the fractional perturbation in the compressional velocity, $\delta v_P/v_P$, and the perturbations in the earthquake hypocentral parameters (origin time, longitude, latitude, and depth). For technical aspects of the inversion, see (*29*).

Subducted lithospheric slabs are large features that cause little or no wavefront healing. Our slab images are in good agreement with earlier studies; therefore, we restrict our analysis to the newly imaged plumes.

As in every high-resolution tomographic study, the fact that we have far more data than unknowns does not guarantee that every model parameter is well resolved. Much of our effort has been spent on determining which of the imaged plume features are reliable. Lack of resolution may take different forms: (i) An ex-

Table 1. Summary of the results for the 32 hotspots present in our tomographic images. Depth limits and minimum radius (in lower mantle unless the plume is confined to the upper mantle) have been determined from the resolution analysis (*29*). Code for plate names: af, African plate; an, Antarctic plate; au, Australian plate; eu, Eurasian plate; nz, Nazca plate; pa, Pacific plate; sa, South American plate.

Label	Name	Latitude and longitude		Plate	Depth (km)*	Radius (km)†	Remarks
AF	Afar	7°N	39°E	af	≥1450	200	Could be a deep plume
AR	Atlantic Ridge	15° & 25°N	45°W	na	~1900	200	Lack of resolution at the base of the mantle gives rise to horizontal smearing
AS	Ascension	8°S	14°W	sa	~2800	100	Robust
AZ	Azores	38°N	26°W	eu	~2800	300	Lack of mid-mantle resolution may be responsible for merging with Canary
BV	Bouvet	54°S	3°E	af	≤1450	400	Connection to African superplume is not well resolved
BW	Bowie	53°N	136°W	pa	≤650	100	Plume wider than 100 km would be visible beneath 300 km depth
CN	Canary	28°N	18°W	af	~2800	400	Robust
CV	Cape Verde	15°N	24°W	af	≥1900	300	Lack of resolution in the deep mantle
CR	Caroline	3°N	167°E	pa	≥1000	300	Lack of resolution at the bottom of the mantle
CC	Cocos/Keeling	17°S	95°E	au	≤1000	200	Nearby plumes strong only in the upper mantle
CK	Cook Island	22°S	158°W	pa	≥1450	200	Lack of resolution in the lower mantle beneath nearby plumes
CS	Coral Sea	15°S	155°E	au	~2800	300	Robust, does not reach the surface, stops at 1450 km depth
CZ	Crozet	46°S	50°E	an	~2350	400	Vertical leakage present, but confined above 1450 km depth; same origin as Kerguelen at 2350 km depth; synthetic plumes are separated down to 1000 km depth
ES	Easter	27°S	108°W	nz	~2800	400	Robust
EA	East Australian	41°S	146°E	au	~650	100	Robust
EF	Eifel	50°N	4°E	eu	~650	100	Robust
ET	Etna	38°N	15°E	eu	≤1000	200	Strong only in the upper mantle
SL	East of Solomon	5°S	165°E	pa	~1000	—	Nearby plumes robustly resolved
GL	Galapagos	0°	92°W	nz	≤1000	300	Strong only in the upper mantle
HN	Hainan	20°N	110°E	eu	~1000	200	Robust
HW	Hawaii	19°N	155°W	pa	≥2350	300	Not enough constraint on depth
IC	Iceland	64°N	17°W	na	≤1000	100	Strong only in the upper mantle (see discussion in text)
IO	Indian Ocean	35°S	100°E	au	≥1900	400	Not well resolved
JF	Juan de Fuca/Cobb	46°N	130°W	pa	≤1000	100	Strong only in the upper mantle
JZ	Juan Fernandez	34°S	81°W	nz	≥1450	300	Lack of resolution below 2350 km depth in the nearby plumes
KG	Kerguelen	50°S	69°E	an	~2350	400	Robust
LS	Louisville	54°S	141°W	pa	≥1000	300	Very weak, newly discovered anomalies located at 55°S, 150°W, and 60°S, 120°W
RN	Reunion	21°S	56°E	af	≥1900	200	Could be a *D*″ plume
SM	Samoa	15°S	168°W	pa	~2800	200	Robust, except between 1000 and 1450 km depth
SJ	South of Java	12°S	112°E	au	~2800	300	Does not reach the surface, stops at 1450 km depth
SY	Seychelles	5°S	56°W	af	~650	—	Nearby plumes robustly resolved
TH	Tahiti	18°S	148°W	pa	~2800	300	Robust, except between 1000 and 1450 km depth

*See text for explanation, including meaning of symbols. †Minimum radius of the plume constrained from the resolution tests.

isting plume may not be imaged with sufficient contrast over its full length, or to its source at large depth, where resolution often decreases; (ii) the regularization may spread a shallow anomaly to larger depth in the image ("leakage"); and (iii) the regularization leads to horizontal "smearing" of an anomaly, resulting in a larger anomaly image with a smaller amplitude than present in Earth.

The resolution tests we have undertaken enable us to determine the minimum radius that a real plume must have for it to be visible in our tomographic images. This minimum plume radius is listed in Table 1. The imaged plume radii should be seen as generous upper limits; because of the limitations to the resolving power combined with the effects of smoothing, the actual plume radii may be much smaller. The depth listed in Table 1 is the deepest level at which the absolute contrast $|\delta v_P/v_P|$ exceeds 0.3%. We code these maximum depths in Table 1 with "≥" whenever we conclude from the resolution tests that the absence of a plume at greater depth may be due to a lack of resolution, or with "≤" whenever there is a possibility that the image is generated by leakage to this depth. In cases where we determined that the resolving power is sufficient, we added "~" to emphasize that the depths in Table 1 are only estimates. Even in the case of well-resolved plumes, the depths are uncertain to several hundred km, particularly in the deepest mantle. This codification of depth values in Table 1 is somewhat incomplete in the sense that resolution may depend on the unknown width of the plume. See (*29*) for more extensive resolution information.

Deep plumes. To emphasize features, including deep plumes that are vertically continuous over all or much of the lower mantle, we compute a vertical average of the P velocity anomaly $\delta v_P/v_P$ in the lowest part of the mantle (1800 to 2800 km depth) (Fig. 1). The African superplume extends high enough to survive this averaging over 1000 km, and is visible as the large low-velocity anomaly beneath southern Africa. Inspection of the unaveraged tomographic model shows that the superplume extends locally upward to depths of 1500 km, in accordance with previous observations (*32*, *33*). This anomaly is part of a broad low-velocity region that underlies the Atlantic, the African continent, and much of Europe. The broad anomaly in the lower mantle beneath the Pacific Ocean, south of the equator, is different in character. Here there are several large velocity anomalies enhanced by the averaging, which can be identified as individual plumes rising from the "superplume": beneath the Coral Sea (15°S, 155°E), east of the Solomon Islands (5°S, 165°E), beneath Samoa (15°S, 168°W), and a broad anomaly centered beneath Tahiti (18°S, 148°W).

North of the equator, the lower mantle beneath the Pacific plate exhibits several high-velocity anomalies forming a ring that extends beneath East Asia and the eastern part of the Indian Ocean. In the unaveraged model, fast anomalies with perturbations greater than 1% are observed beneath Tonga and Asia, the latter presumably caused by the subduction of the Tethys slab (*34*–*39*). Together, these form a ring of high-velocity anomalies around the Pacific, which reaches down to the D'' region. Finally, the polar regions are characterized by lower mantle of opposite velocity anomaly at all longitudes; if we assume that these anomalies mainly reflect temperatures, then the deep mantle is hot beneath the North Pole but cold beneath Antarctica. This suggests that the large J_3 coefficient in the geoid [the "pear" shape of Earth (*40*)] may be caused by this deep-seated bipolar anomaly.

The Ascension, Azores, Canary, Easter, Samoa, and Tahiti hotspots all have well-resolved deep-rooted origins near the bottom of the mantle (Fig. 2) (figs. S2 to S9). Ascension and St. Helena (fig. S2) merge at about 1000 km depth, a well-resolved confluence that is observed for several other deep plumes. For example, Azores and Canary (fig. S3) are distinct plumes down to 1450 km depth, where they merge together and begin to bend eastward to reach the bottom of the mantle at about 30°N, 10°W. Farther south, but less well resolved, the Cape Verde (fig. S3) plume joins this complex at 1900 km depth. Kerguelen (fig. S7) and Crozet (fig. S4) are seen to originate from a common broad anomaly located north of Crozet at 2350 km depth; the width of this anomaly is affected by horizontal smearing. Beneath the Pacific superswell, the Tahiti, Cook Island, and Samoa plumes (figs. S8 and S9) are closely spaced. The images for the Tahiti and Samoa plumes are robust and show independent features to large depth in the mantle. Cook Island merges with Tahiti at about 1450 km depth, although we cannot rule out that this is an artifact caused by lack of resolution.

Hawaii (fig. S6) is one of the longest lived plumes and is by far the strongest in flux, as measured by the topographic swell it creates (*1*, *2*); the associated fast anomaly in our model falls somewhat short of expectations.

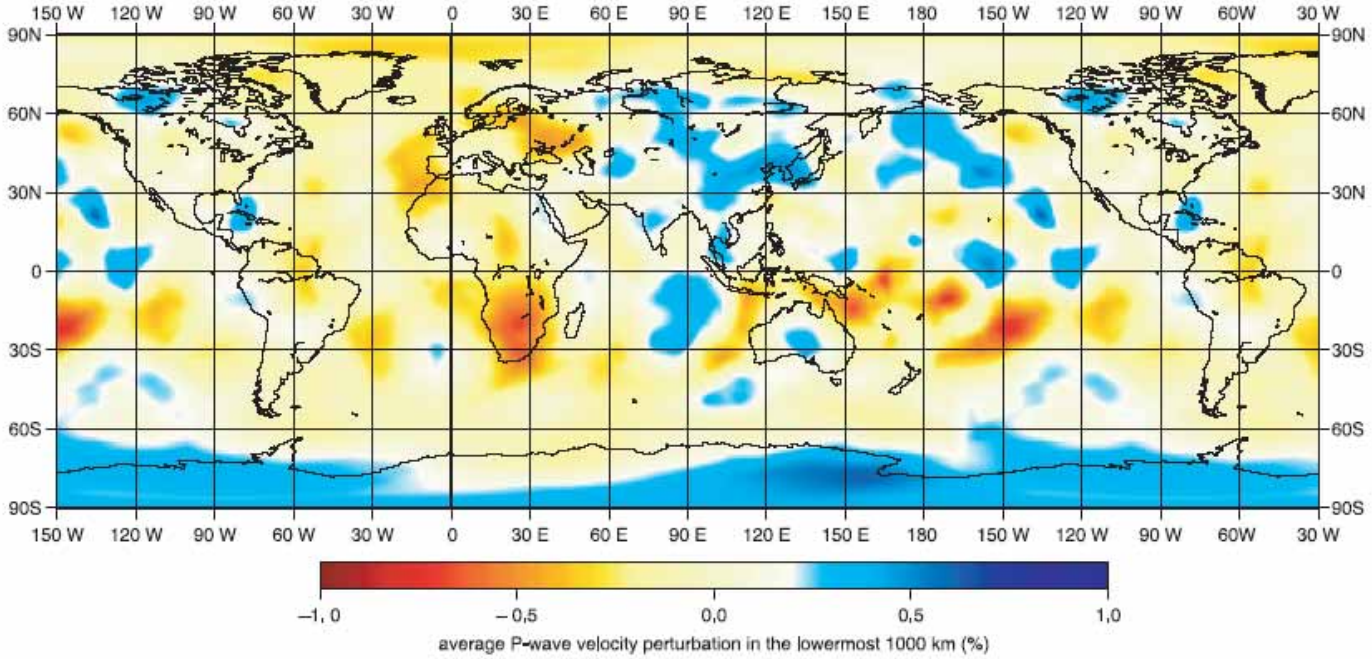

Fig. 1. Vertical average over the lowermost 1000 km of the mantle of the relative velocity perturbation $\delta v_P/v_P$. The averaging emphasizes features that are continuous with depth. Map has been wrapped around to have complete views of both the Atlantic and the Pacific oceans.

This is most likely due to the dearth of seismic ray paths sampling this structure at mid-mantle depth, due to the distance of Hawaii from the circum-Pacific seismicity. Seismic rays from the Tonga subduction zone to North American stations are abundant, but these pass southeast of the suspected plume location near the core-mantle boundary. Resolution analysis indicates that only a very wide plume of radius >300 km would be clearly resolved. In a separate inversion using only low-frequency data (which sense a wider region around the ray), the Hawaii plume anomaly extends to 2800 km depth (*24*).

Afar, Juan Fernandez (fig. S5), Cook Island (figs. S8 and S9), Caroline, Reunion, and two newly discovered anomalies near Louisville could also be deep plumes (fig. S1). Our resolution analysis shows that narrow plumes beneath these hotspots suffer a loss of resolution at increasing depth, making any deep plumes invisible.

Shallow plumes. A relatively large number of plumes are clearly imaged only in the upper mantle: Bowie, Eastern Australia, Eifel, Etna, Iceland, Cocos-Keeling, Galapagos, and Juan de Fuca/Cobb (Fig. 3) (figs. S10 to S16). Eastern Australia (fig. S12) and Eifel (fig. S13) show robust velocity anomalies clearly constrained down to 650 km depth. Bowie and Juan de Fuca/Cobb (fig. S10) are connected to form a broad low-velocity anomaly at 300 km. Bowie, which is visible only down to 300 km depth, is not really identifiable as an isolated plume. Juan de Fuca/Cobb reaches 1000 km depth; however, the velocity perturbation at this depth is much weaker than in the upper mantle, and it is unlikely that the source region of the Juan de Fuca/Cobb hotspot is at a depth of 1000 km or greater. An origin shallower than 1000 km is also suggested for Cocos/Keeling (fig. S16), Etna (fig. S13), Galapagos (fig. S14), and Iceland (fig. S15). At about 650 km, Etna shows a connection to a plume-like low-velocity anomaly beneath the Gulf of Suez.

In our images, the very strong upper-mantle plume beneath Iceland has almost disappeared at 1000 km depth. Vertical leakage down and below this depth could easily explain the weak lower-mantle anomaly of −0.3%. We suspect that such leakage has led an earlier study to suggest a deep plume (*41*). It is clear from our image that the strong velocity anomaly observed in the upper mantle beneath Iceland is not generated by a large upwelling from the lower mantle.

A large drop in the temperature dependence of v_p in the transition zone (*42*) could make plumes a much weaker velocity anomaly in the lower mantle and therefore more difficult to image, leading to apparent source regions near 670 km. However, the fact that we do observe numerous plumes extending to the deep mantle weakens this argument, at least as a phenomenon affecting the stronger upper-mantle plumes.

Newly discovered plumes. Several new velocity anomalies that we associate with plumes are visible in our model and are not related to well-known hotspots. A Mid-Atlantic ridge plume is identifiable with anomalies at 12°N and 25°N (fig. S1); an axial hotspot at this location has recently been hypothesized (*43*). A deep plume stops at about 1450 km depth south of Java (Fig. 3) (fig. S16). An anomaly feeding the Southeast Indian ridge (fig. S1) is defined down to 2350 km depth, where it merges with the anomaly located south of Java. The resolution tests indicate that all of these structures are robust. The deep plume beneath the Coral Sea (Fig. 3) (fig. S11) extends upward to 2350 km, with a weak connection to a newly discovered plume beneath East Solomon (5°S, 165°E) (Fig. 3) (fig. S11). The East Solomon plume extends upward to 1000 km, where a weak connection is visible with a plume beneath the Caroline Islands (Fig. 3). The Louisville hotspot, characterized by a well-delineated narrow island chain, has waned in recent geological times. We do not observe a plume beneath either of the disputed present-day locations (*1*, *44*). Instead, we recover two weak low-velocity anomalies situated to the northwest and southeast of the Louisville hotspot (fig. S1), which we list as "Louisville" in Table 1. Finally, we image a hitherto unreported plume north of Reunion, approximately beneath the Seychelles (5°S, 56°E) (fig. S1). This plume extends down to 650 km and is well resolved. We note that Seychelles is a continen-

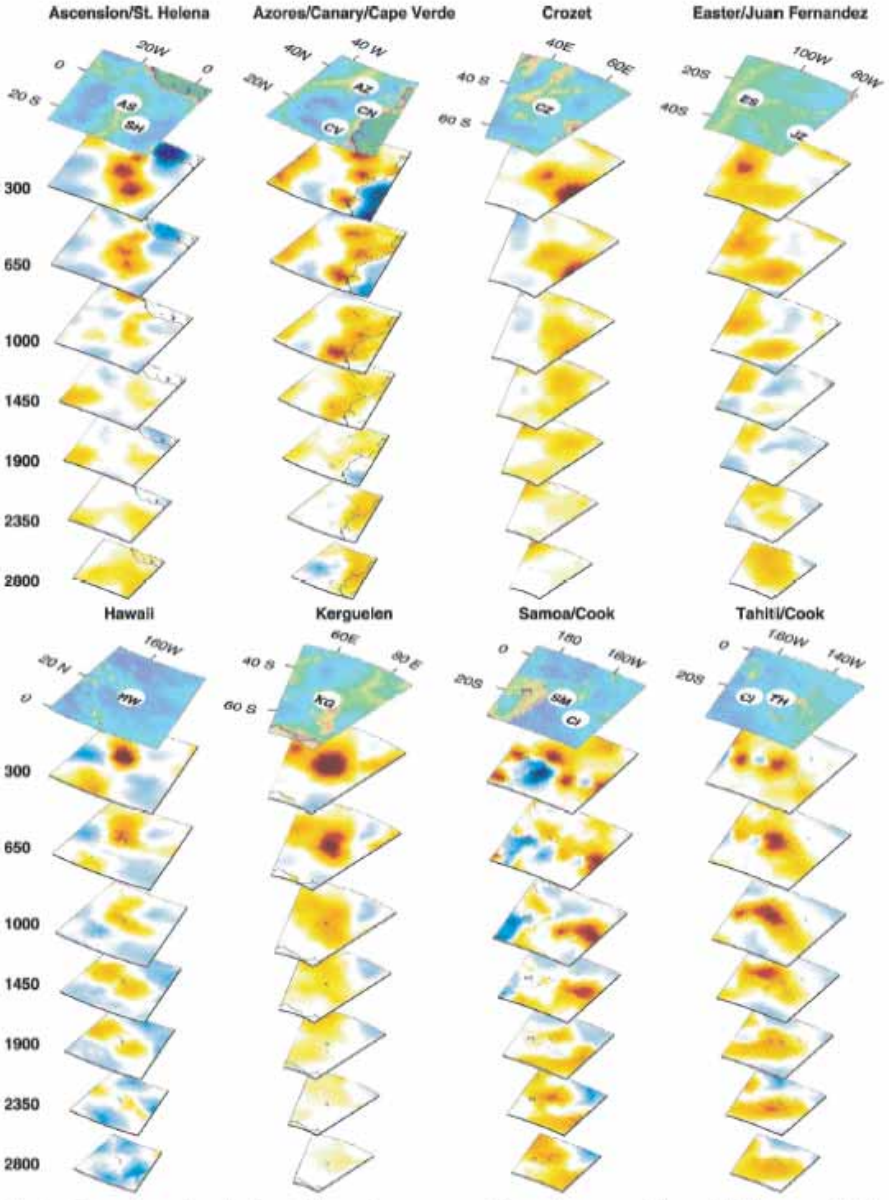

Fig. 2. Three-dimensional view of deep plumes present in our tomographic model. Maps are 40° by 40°, appropriately scaled with depth. Note the vertical exaggeration. The depth spacing changes at 1000 km. The color scale is the same as in Fig. 3. Two-letter identifiers show hotspot locations.

tal fragment left behind from the breakup of Gondwana, and not a conventional oceanic island (*45*).

Absent plumes. A number of proposed plumes (*1*, *2*, *9*) do not exhibit associated velocity anomalies in our images. Our resolution tests show that even a 0.3% anomaly of only 100 km radius would be visible beneath Yellowstone, indicating that there is not a substantial plume. Guadalupe is not an isolated low-velocity anomaly in our tomographic image, but is rather part of a broad low-velocity region connecting Bowie, Juan de Fuca/Cobb, and what seems to be a signature of the East Pacific Rise (15°N, 115°W), that is, south of Guadalupe. Perhaps because of the absence of a co-sited station, we do not resolve a plume in the upper mantle beneath Macdonald Island.

Implication for mantle dynamics. Our *P*-wave velocity images show unambiguous evidence that at least nine hotspots cap a plume originating near the core-mantle boundary. However, at least another eight are associated with plumes whose imaged base lies near the 670-km discontinuity. Although the phase transition at 670 km has been a candidate for a second thermal boundary layer, recent tomographic evidence (*34*, *35*) for whole-mantle convection had made this less likely. Yet if the 670-km discontinuity can temporarily delay penetration, upwelling material may accumulate and give rise to an apparent source region at or just below 670 km (*15*). The coexistence of at least two preferred depths where our plumes images stop is suggestive of the existence of at least two convecting regions, symbiotically linked in a regime that is more complex than either the whole-mantle or layered convection models. It is, however, also possible that the variety of plume styles we image is simply a manifestation of the expected intermittency and ephemerality of high–Rayleigh number, whole-mantle convection.

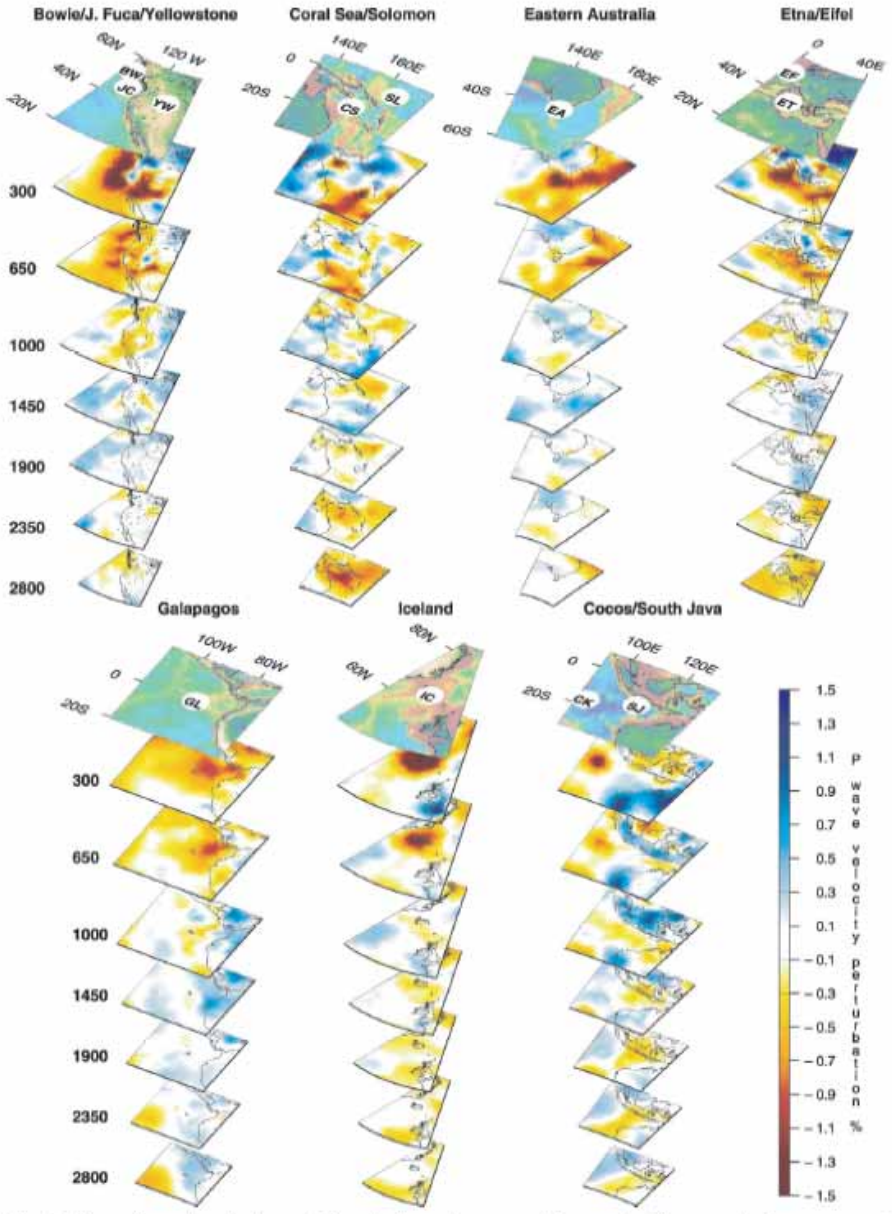

Fig. 3. Three-dimensional views of the shallow plumes and the newly discovered plumes present in our velocity model. Plotting format, including change in depth spacing at 1000 km, is identical to that of Fig. 2.

Our tomographic images also show plume images that fade at mid-mantle depths. From a geodynamical point of view, steady, nonintermittent plumes that do not originate near 670 km or near the *D″* layer are problematic, because no thermal boundary layer has so far been observed in the mid-mantle. The presence of a change in mantle chemistry has been postulated to explain changes in the pattern of subduction (*34*, *35*, *46*) and the presence of an anticorrelation between *P*-wave and *S*-wave velocity in the lower mantle (*47*). Anderson (*48*) advocates a transition at a depth near 1000 km. So far, the presence of such a mid-mantle transition has not been confirmed (*49*, *50*). A geochemical model has been proposed with a thermal boundary layer in the mid-mantle, which is strongly varying in depth and seismically invisible (because compositional changes compensate for the higher temperature, keeping velocities approximately the same) (*51*). Laboratory experiments show that thin plumes can arise from such a deep layer (*11*); however, we observe thicker plumes (Table 1). Tackley's model (*52*) identifies the deep layer with the location of the superplumes, which is not where we observe the fading of the plume images. The simplest explanation for the plume images extending only to mid-mantle depths is that they are really deep-mantle plumes, which are not resolved at deeper levels. Alternatively, we could be observing a large number of hiatuses in plume flux; however, the fact that we see many more plume tails than plume heads around these depths makes this less probable on statistical grounds.

The plumes must have diameters of several hundred km, or they would not have been resolved even with our improved imaging techniques. Because of the very low efficiency of heat diffusion, the thermal "halo" around the plume is only a fraction of the width (typically 50 km for a plume that has been active for 100 million years). Thus, plumes must be wider than is commonly assumed, and this provides qualitative information about the rheology in the lower mantle. Although a Newtonian viscosity for the upper mantle seems to be required by the modeling of glacial rebound observations, the rheology of the lower mantle is not well constrained by surface observations (*53*). However, the wide plumes we observe would clearly be favored by a lower mantle with a sluggish convective regime such as would be

expected for a high, Newtonian viscosity (*54*).

Of course, our images only provide a snapshot of the current mantle, and we are unable to infer the rise velocity of the plumes. Because of this, we are unable to place a firm constraint on the heat flux carried by the plumes; however, an order-of-magnitude calculation indicates that the observed heat flux of about 44 TW at Earth's surface imposes a limit on the rise velocity of the plumes, which is probably below 10 cm/year (*55*). This loose constraint reinforces our conclusion that convection in the lower mantle is slow, and indicates that the role of plumes in transporting heat from the core to the surface of the Earth is larger than previously suggested (*1*).

Another surprising observation is the lack of correlation between the maximum depth of a plume image and the associated ^{3}He/^{4}He anomaly. Of the ocean islands with high values of ^{3}He/^{4}He (*3*), Easter, Hawaii, Kerguelen, Samoa, and Tahiti are well-resolved deep plumes (Table 1). Afar, Cape Verde, Caroline, Reunion, and Jean Fernandez are potential *D″* plumes and also have correspondingly high ^{3}He/^{4}He. But other plumes for which a deep origin can be decisively ruled out (Galapagos, Iceland) have high ^{3}He/^{4}He. Conversely, St. Helena and Canary Islands have a low ^{3}He/^{4}He ratio but have anomalous velocities that extend deeply into the mantle.

The maximum velocity anomaly of the observed plumes in the lower mantle is reduced by a factor of about 3 with respect to the value found in the upper mantle (which is often in excess of −1.5%). Even though the magnitude of each plume anomaly is affected by the resolution, this diminution of $\delta v_P/v_P$ with depth is in accordance with predictions of dv_P/dT (*42*).

References and Notes

1. N. H. Sleep, *J. Geophys. Res.* **95**, 6715 (1990).
2. G. F. Davies, *J. Geophys. Res.* **93**, 10467 (1988).
3. V. Courtillot, A. Davaille, J. Besse, J. Stock, *Earth Planet. Sci. Lett.* **205**, 295 (2003).
4. J. T. Wilson, *Can. J. Phys.* **41**, 863 (1963).
5. J. T. Wilson, *Philos. Trans. R. Soc. London* **258A** (1965).
6. W. J. Morgan, *Nature* **230**, 42 (1971).
7. W. J. Morgan, *Geol. Soc. Am. Mem.* **132**, 7 (1972).
8. M. A. Richards, R. A. Duncan, V. E. Courtillot, *Science* **246**, 103 (1989).
9. V. Courtillot, C. Jaupart, I. Manighetti, P. Tapponier, J. Besse, *Earth Planet. Sci. Lett.* **166**, 177 (1999).
10. I. O. Norton, *The History and Dynamics of Global Plate Motions* (Geophysical Monograph 121, American Geophysical Union, Washington, DC, 2000), pp. 339–357.
11. A. Davaille, *Nature* **402**, 756 (1999).
12. A. Davaille, F. Girard, M. L. Bars, *Earth Planet. Sci. Lett.* **203**, 621 (2002).
13. H.-P. Bunge, M. A. Richards, J. R. Baumgardner, *J. Geophys. Res.* **102**, 11991 (1997).
14. S. Zhong, M. T. Zuber, L. Moresi, M. Gurnis, *J. Geophys. Res.* **105**, 11063 (2000).
15. L. Cserepes, D. A. Yuen, *Earth Planet. Sci. Lett.* **183**, 61 (2000).
16. D. L. Anderson, *The Core-Mantle Boundary Region* (American Geophysical Union, Washington DC, 1998), pp. 255–271.
17. D. L. Anderson, *Geophys. Res. Lett.* **27**, 3623 (2000).
18. G. R. Foulger, J. H. Natland, *Science* **300**, 921 (2003).
19. F. A. Dahlen, S.-H. Hung, G. Nolet, *Geophys. J. Int.* **141**, 157 (2000).
20. S.-H. Hung, F. A. Dahlen, G. Nolet, *Geophys. J. Int.* **141**, 175 (2000).
21. Y. A. Kravtsov, Y. I. Orlov, *Geometrical Optics of Inhomogeneous Media* (Springer-Verlag, New York, 1990).
22. G. Nolet, F. A. Dahlen, *J. Geophys. Res.* **105**, 19043 (2000).
23. S.-H. Hung, F. A. Dahlen, G. Nolet, *Geophys. J. Int.* **146**, 289 (2001).
24. R. Montelli, G. Nolet, G. Masters, F. A. Dahlen, S.-H. Hung, *Geophys. J. Int.*, in press.
25. H.-C. Nataf, J. VanDecar, *Nature* **364**, 115 (1993).
26. The dominant periods of travel times in the bulletins are poorly documented and vary among stations, but are commonly obtained from instruments that are sensitive to a narrow band of frequencies around 1 Hz.
27. H. Bolton, G. Masters, *J. Geophys. Res.* **106**, 13527 (2001).
28. H. Bolton, thesis, University of California, San Diego (1996).
29. See supporting data on *Science* Online.
30. E. R. Engdahl, R. D. van der Hilst, R. Buland, *Bull. Seismol. Soc. Am.* **88**, 722 (1998).
31. A. Morelli, A. M. Dziewonski, in *Seismic Tomography*, G. Nolet, Ed. (Reidel, Dordrecht, Netherlands, 1987), pp. 251–274.
32. J. Ritsema, S. Ni, D. V. Helmberger, H. P. Crotwell, *Geophys. Res. Lett.* **25**, 4245 (1998).
33. S. Ni, E. Tan, M. Gurnis, D. Helmberger, *Science* **296**, 1850 (2002).
34. R. D. van der Hilst, S. Widiyantoro, E. R. Engdahl, *Nature* **386**, 578 (1997).
35. S. P. Grand, R. D. van der Hilst, S. Widiyantoro, *GSA Today* **7**, 1 (1997).
36. S. P. Grand, *J. Geophys. Res.* **99**, 11591 (1994).
37. H. Bijwaard, W. Spakman, E. R. Engdahl, *J. Geophys. Res.* **103**, 30055 (1998).
38. R. Van der Voo, W. Spakman, H. Bijwaard, *Nature* **397**, 246 (1999).
39. Y. J. Gu, A. M. Dziewonski, W. Su, G. Ekström, *J. Geophys. Res.* **106**, 11169 (2001).
40. J. O'Keefe, A. Eckels, R. Squires, *Science* **129**, 565 (1959).
41. H. Bijwaard, W. Spakman, *Earth Planet. Sci. Lett.* **166**, 121 (1999).
42. S.-I. Karato, *Geophys. Res. Lett.* **20**, 1623 (1993).
43. N. H. Sleep, *Geochem. Geophys. Geosyst.* **3**, 10.1029/2001GC00290 (2002).
44. W. J. Morgan, personal communication.
45. A. Wegener, *The Origin of Continents and Oceans* (Methuen, London, 1924).
46. R. D. van der Hilst, H. Kárason, *Science* **283**, 1885 (1999).
47. W.-J. Su, A. M. Dziewonski, *Phys. Earth Planet. Inter.* **100**, 135 (1997).
48. D. L. Anderson, *Science* **293**, 2016 (2001).
49. J. E. Vidale, G. Schubert, *Geophys. Res. Lett.* **28**, 859 (2001).
50. D. W. Vasco, L. R. Johnson, O. Marques, *J. Geophys. Res.* **108**, 2022 (2003).
51. L. H. Kellogg, B. H. Hager, R. D. van der Hilst, *Science* **283**, 1881 (1999).
52. P. J. Tackley, *Science* **288**, 2002 (2000).
53. P. Wu, *Geophys. J. Int.* **139**, 691 (1999).
54. P. van Keken, *Earth Planet. Sci. Lett.* **148**, 1 (1997).
55. For example, if we integrate ΔT at 800 km depth over the total area for which $\delta v_P/v_P < -0.5\%$ (ΔT = 100 K) using $d \ln V_P/dT = -0.51 \times 10^{-4}$ K^{-1}, a heat capacity c_p = 1270 J kg^{-1} K^{-1}, a density ρ = 4450 kg m^{-3}, and a rise velocity of 1 cm/year, we obtain an advective heat flux of 9.8 TW. The estimate scales linearly with the assumed rise velocity. Smoothing does not influence the flux itself, but may underestimate the area confined by the −0.5% isosurface, so this is a conservative estimate that could easily be larger. Imposing a different limit (e.g., 0.7% or 140 K) brings the flux down to 3.1 TW for 1 cm/year.

56. We thank J. Morgan for numerous discussions and helpful suggestions. Supported by NSF grants EAR-9814570 and EAR-0105387.

Supporting Online Material

www.sciencemag.org/cgi/content/full/1092485/DC1
SOM Text
Figs. S1 to S21
References

10 October 2003; accepted 18 November 2003
Published online 4 December 2003;
10.1126/science.1092485
Include this information when citing this paper.

ATP-Driven Exchange of Histone H2AZ Variant Catalyzed by SWR1 Chromatin Remodeling Complex

Gaku Mizuguchi,* Xuetong Shen,*† Joe Landry,* Wei-Hua Wu,‡ Subhojit Sen,‡ Carl Wu§

The conserved histone variant H2AZ has an important role in the regulation of gene expression and the establishment of a buffer to the spread of silent heterochromatin. How histone variants such as H2AZ are incorporated into nucleosomes has been obscure. We have found that Swr1, a Swi2/Snf2-related adenosine triphosphatase, is the catalytic core of a multisubunit, histone-variant exchanger that efficiently replaces conventional histone H2A with histone H2AZ in nucleosome arrays. Swr1 is required for the deposition of histone H2AZ at specific chromosome locations in vivo, and Swr1 and H2AZ commonly regulate a subset of yeast genes. These findings define a previously unknown role for the adenosine triphosphate–dependent chromatin remodeling machinery.

The condensation of eukaryotic DNA in arrays of nucleosomes has a profound effect on gene function. To counteract constraints imposed by nucleosome structure, cells deploy two major classes of multiprotein enzymes, which covalently modify the nucleosome core histones or catalyze nucleosome mobility in an adenosine triphosphate (ATP)–dependent fashion (*1*–*5*). Much of our current understanding of these processes is derived